Applied Catalysis B: Environmental 227 (2018) 512–518

Contents lists available at ScienceDirect

Applied Catalysis B: Environmental

journal homepage: www.elsevier.com/locate/apcatb

$AgIn_5S_8$ nanoparticles anchored on 2D layered $ZnIn_2S_4$ to form 0D/2D heterojunction for enhanced visible-light photocatalytic hydrogen evolution

Zhongjie Guan[a,b,*], Zhiqiang Xu[a,c], Qiuye Li[a,**], Peng Wang[a], Guoqiang Li[b], Jianjun Yang[a,**]

[a] National & Local Joint Engineering Research Center for Applied Technology of Hybrid Nanomaterials, Collaborative Innovation Center of Nano Functional Materials and Applications of Henan Province, Henan University, Kaifeng 475004, China
[b] Key Laboratory of Photovoltaic Materials of Henan Province, School of Physics & Electronics, Henan University, Kaifeng 475004, China
[c] School of Pharmacy, Jining Medical University, Jinning 272000, China

ARTICLE INFO

Keywords:
0D/2D Heterojunction
$AgIn_5S_8$ nanoparticles
2D Layered $ZnIn_2S_4$
Solar hydrogen generation
Charge seperation

ABSTRACT

Constructing a 0D/2D heterojunction is an important way to ameliorate the charge separation for achieving efficient solar hydrogen production. In this study, zero-dimensional (0D) $AgIn_5S_8$ nanoparticles/two-dimensional (2D) layered $ZnIn_2S_4$ 0D/2D heterojunction composite was designed and prepared via a facile two-step hydrothermal process. Anchoring the $AgIn_5S_8$ nanoparticles on the 2D layered $ZnIn_2S_4$ can shorten the charge-migration distance, provide abundant active sites and extend the visible-light absorption. Benefiting from those favorable properties, the $AgIn_5S_8/ZnIn_2S_4$ 0D/2D heterojunction composite exhibits the highest H_2 evolution rate of 949.9 μmol g^{-1} h^{-1} under visible light irradiation ($\lambda > 420$) when the weight ratio of $AgIn_5S_8$ to $ZnIn_2S_4$ is 30%, which is about 3.6 and 17.6 times higher than pure $ZnIn_2S_4$ and $AgIn_5S_8$, respectively. Photoluminescence (PL) and photocurrent response results indicate that the improved charge separation efficiency is a critical reason for the enhanced H_2 evolution activity. This study suggests that constructing a 0D/2D heterojunction can provide an efficient way to improve the photocatalytic performance of semiconductor photocatalysts for solar hydrogen production.

1. Introduction

Converting the abundant solar energy into hydrogen is a promising strategy for solving the growing global energy demand [1,2]. Solar water splitting using semiconductor photocatalyst is considered to be one of the economical and effective technology to produce H_2 [3]. Since Fujishima found that TiO_2 could split water into hydrogen under light irradiation, tremendous efforts have been dedicated to exploit efficient photocatalysts [4–6]. Recently, ternary $ZnIn_2S_4$ has attracted much attention due to its suitable band gap (~2.4 eV) and nontoxicity [7–9]. However, the photocatalytic performance of pure $ZnIn_2S_4$ is seriously restricted by the fast photogenerated charge recombination and relatively narrow visible light utilization range (< about 530 nm). In order to solving these drawbacks, constructing heterojunction by coupling with another multi-functional photocatalyst is a commonly used method, such as hybridization with TiO_2, CdS and C_3N_4 [10–12]. Usually, the morphology of heterojunction also plays an important role for improving the photogenerated charge separation [13,14]. However, the morphology of $ZnIn_2S_4$-based heterojunction and the relatively narrow visible light utilization range of $ZnIn_2S_4$ are seldom considered at the same time in previous studies. Therefore, tailoring the morphology and band gap of the integrating semiconductor photocatalyst is very important to improve the hydrogen evolution performance of $ZnIn_2S_4$.

Among various photocatalysts, $AgIn_5S_8$ has been proven to be an efficient photocatalyst for solar H_2 production [15,16]. In addition to this, $AgIn_5S_8$ has the relatively narrow band gap (~1.7 eV), which can efficiently utilize the wide spectrum of sunlight. Lately, 0D/2D heterojunction has received considerable attention because of its distinguished properties [13,17,18]. 0D nanoparticle has the advantages of short charge-migration distance and large surface area, while 2D nanosheet can serve as a support providing more contact areas and avoiding the self-aggregation of 0D nanoparticles. Ran et al reported that the $Zn_xCd_{1-x}S$ nanoparticles/phosphorene nanosheets 0D/2D heterojunction composite showed higher H_2 evolution activity than pure $Zn_xCd_{1-x}S$ [19]. A 0D/2D heterojunction composite of CdZnS quantum dots/g-C_3N_4 nanosheets was prepared by Yao et al. and exhibited excellent H_2 production activity [20]. Therefore, it is highly desired that

* Corresponding author at: National & Local Joint Engineering Research Center for Applied Technology of Hybrid Nanomaterials, Collaborative Innovation Center of Nano Functional Materials and Applications of Henan Province, Henan University, Kaifeng 475004, China.
** Corresponding authors.
E-mail addresses: guanzj@henu.edu.cn (Z. Guan), qiuyeli@henu.edu.cn (Q. Li), yangjianjun@henu.edu.cn (J. Yang).

https://doi.org/10.1016/j.apcatb.2018.01.068
Received 22 November 2017; Received in revised form 5 January 2018; Accepted 28 January 2018
Available online 31 January 2018
0926-3373/

constructing $AgIn_5S_8$ nanoparticles/$ZnIn_2S_4$ nanosheets 0D/2D heterojunction to overcome the fast charge recombination and low visible light utilization in $ZnIn_2S_4$ simultaneously.

In this study, we designed and prepared the $AgIn_5S_8$ nanoparticles/$ZnIn_2S_4$ nanosheets 0D/2D heterojunction composite by a facile two-step hydrothermal process and the H_2 evolution performance of the composite photocatalysts were evaluated. To the best of our knowledge, this is the first report about $AgIn_5S_8/ZnIn_2S_4$ 0D/2D heterojunction composite for solar H_2 production from water. The $AgIn_5S_8/ZnIn_2S_4$ 0D/2D heterojunction composite exhibits much higher H_2 evolution activity than the pure $ZnIn_2S_4$ and $AgIn_5S_8$, respectively. In addition, the $AgIn_5S_8/ZnIn_2S_4$ composite presents stability for photocatalytic hydrogen evolution in the consecutive three cycles. The detail mechanism of enhanced H_2 production performance for the $AgIn_5S_8/ZnIn_2S_4$ 0D/2D heterojunction composite was also investigated.

2. Experimental section

2.1. Synthesis of $ZnIn_2S_4$ photocatalysts

The $ZnIn_2S_4$ photocatalysts were prepared by a hydrothermal method [21]. In a typical experiment, 0.136 g $ZnCl_2$, 0.586 g $InCl_3{\cdot}4H_2O$ and 0.46 g thioacetamide (TAA) was dissolved into 60 mL deionized water under stirring. After that, the mixed solution was transferred into a 100 mL Teflon-lined autoclave and heated at 200 °C for 24 h. After the reaction finished, the yellow $ZnIn_2S_4$ photocatalysts were collected by centrifugation and washed with water and ethanol for three times. Finally, the yellow $ZnIn_2S_4$ powders were dried at 60 °C for 12 h in an vacuum oven.

2.2. Synthesis of $AgIn_5S_8/ZnIn_2S_4$ 0D/2D heterojunction composite photocatalysts

The $AgIn_5S_8/ZnIn_2S_4$ 0D/2D heterojunction composite photocatalysts were prepared by a modified hydrothermal method [22]. In a typical synthesis, 3.9 mg $AgNO_3$, 129.5 mg $In(OAC)_3{\cdot}4.5H_2O$ and excess L-cysteine were added into 22.0 mL deionized water step by step under vigorous stirring. After that, the pH value of the mixed solution was adjusted to 8.5 using NaOH solution. Then 17.3 mL TAA solution (0.05 mol/L) and a certain amount of $ZnIn_2S_4$ powders were added to the above mixed solution under stirring. Finally, the mixed solution was transferred into a 50 mL Teflon-lined autoclave and heated at 110 °C for 5 h. After reaction, the $AgIn_5S_8/ZnIn_2S_4$ composite powders were collected via centrifugation and washed three times with ethanol before dried at 60 °C for 12 h. Pure $AgIn_5S_8$ sample was prepared using the same procedure without adding $ZnIn_2S_4$. In order to obtain an intimate contact between $AgIn_5S_8$ and $ZnIn_2S_4$, the dried $AgIn_5S_8/ZnIn_2S_4$ composite powders were annealed at 300 °C for 2 h under N_2 gas environment. For the purpose of investigate the effect of $AgIn_5S_8$ content on the H_2 production performance, a series of composite samples with different weight ratios of $AgIn_5S_8$ were prepared and labeled as X% $AgIn_5S_8$, where X represents the weight ratio of $AgIn_5S_8$ to $ZnIn_2S_4$ in the composite samples.

2.3. Characterization of photocatalysts

The crystal structures of the photocatalysts were measured through an X-ray diffractometer ((Bruker D8-AVANCE, Germany). The morphologies of the photcatalysts were characterized by SEM (JSM-7001F, FEI Co.) and TEM ((JEM-2100, Japan). The surface chemical states and valence-band XPS spectra of the photocatalysts were recorded using X-ray photoelectron spectroscopy (Thermo ESCALAB 250Xi). The UV–vis diffuse reflectance spectrum (DRS) of the photocatalysts were measured on a UV–vis spectrophotometer (U-3010, Shimadzu). The photoluminescence (PL) spectra of the photocatalysts were recorded using a F-7000 FL spectrophotometer. The excitation light wavelength of 340 nm and 450 nm were chose for $ZnIn_2S_4$ or $AgIn_5S_8/ZnIn_2S_4$ composite and $AgIn_5S_8$, respectively. The Ag ion concentration was measured using inductively coupled plasma atomic emission spectroscopy (ICP-AES, Optima-7300DV, PE, USA). The time-resolved transient PL decay spectra were conducted using an luorescence spectrophotometer (FLS980, England) at room temperature.

2.4. Photoelectrochemical measurement

The working photoelectrodes were prepared as follows: 0.01 g photocatalysts powders were dispersed in 3.5 mL ethanol under ultrasound condition. Then the mixed solution was dropped several times on the ITO substrate. Finally, the prepared photoelectrodes were annealed at 300 °C for 1 h under N_2 gas environment. The photocurrent response curves of the samples were recorded in an electrochemical analyzer (ChenhuaCHI660E, China) using a three electrode system, in which a Pt slice, a saturated calomel electrode (SCE) and the prepared photoelectrode were used as the counter electrode, the reference electrode and the working electrode, respectively. A 300 W Xe lamp equipped with a 420 nm cutoff filter was used as the light source. Na_2SO_4 aqueous solution (0.1 mol/L) was chose as electrolyte.

2.5. Photocatalytic H_2 production

The photocatalytic H_2 evolution reactions were conducted in a sealed Pyrex glass cell (Beijing China Education Au-light Co., Ltd). A 300 W xenon lamp with a cut-off filter ($\lambda > 420$ nm) was used the irradiation light. In a typical photocatalytic H_2 evolution experiment, 50 mg photocatalysts was dispersed into 100 mL deionized water containg 0.25 mol/L Na_2S and 0.25 mol/L Na_2SO_3. 2wt% cocatalyst Pt was introduced via a in-situ photodeposition method using the H_2PtCl_4 aqueous solution. Before reaction, the sealed cell was degassed for about 15 min to exclude the air. The Pt loading process was continued about 4.5 h under visible light irradiation ($\lambda > 420$ nm) and then further degassed until no H_2 can be detected. After that, the amount of evolved H_2 gases with time were measured by an online gas chromatography (GC-7920, TCD, Ar carrier).

3. Results and discussion

3.1. Characterization of photocatalysts

Fig. 1 shows the XRD patterns of pure $ZnIn_2S_4$, $AgIn_5S_8$ and $AgIn_5S_8/ZnIn_2S_4$ composites with different $AgIn_5S_8$ content. For pure

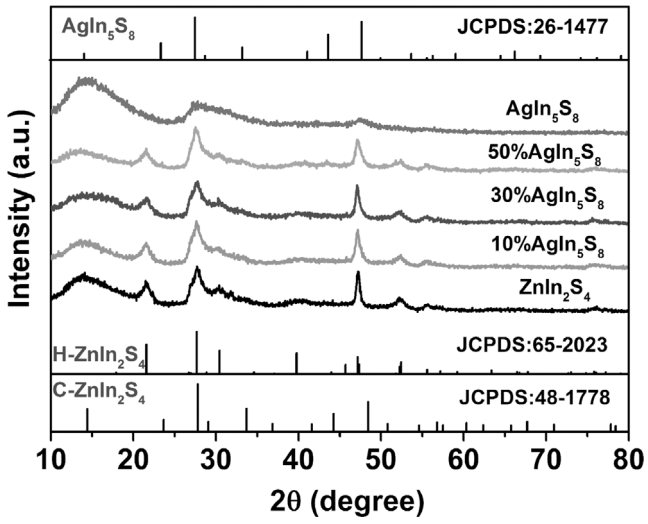

Fig. 1. XRD patterns of pure $ZnIn_2S_4$, $AgIn_5S_8$ and $AgIn_5S_8/ZnIn_2S_4$ composites with different $AgIn_5S_8$ content.

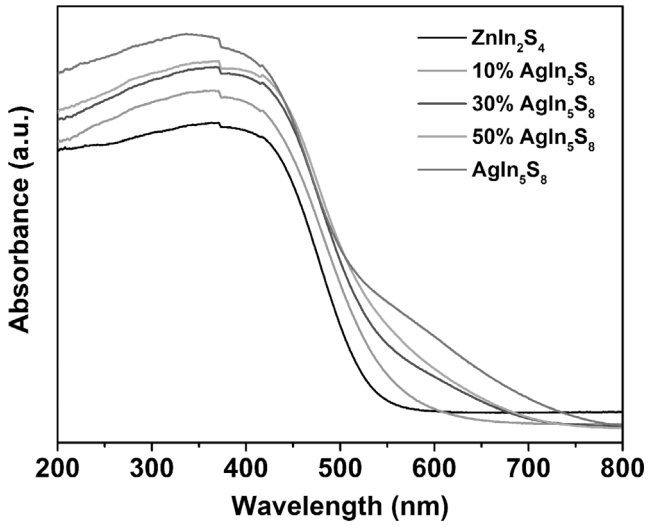

Fig. 2. UV–vis diffuse reflectance spectra of pure $ZnIn_2S_4$, $AgIn_5S_8$ and $AgIn_5S_8/ZnIn_2S_4$ composites with different $AgIn_5S_8$ content.

$ZnIn_2S_4$, there are six strong diffraction peaks at 21.6°, 27.7°, 30.5°, 47.2°, 52.4° and 55.6°, which can be attributed to the (006), (102), (104), (110), (116), and (022) crystal planes of hexagonal $ZnIn_2S_4$ (JCPDS card No. 65-2023), respectively [23]. While another obvious diffraction peak at 14.45° was also observed, which can be assigned to the (111) crystal plane of cubic $ZnIn_2S_4$ (JCPDS card No. 48-1778) [23,24]. The result indicates pure $ZnIn_2S_4$ is a hexagonal and cubic mixed phase. For pure $AgIn_5S_8$, three main broad diffraction peaks at 14.2°, 27.6° and 47.8°correspond respectively to the (111), (311), and (440) crystal plane of cubic $AgIn_5S_8$ (JCPDS card No. 26-1477) [25]. The broad diffraction peaks mean that the $AgIn_5S_8$ has a poor crystal quality due to the low synthetic temperature and short synthetic time. Compared with pure $ZnIn_2S_4$, the XRD patterns of the $AgIn_5S_8/ZnIn_2S_4$ composites with different $AgIn_5S_8$ content show no obvious change. A primary reason is that the main diffraction peaks of $AgIn_5S_8$ are very close to the diffraction peaks of $ZnIn_2S_4$ due to similar crystal structure and thus the main diffraction peaks overlap with each other. Another reason can be ascribed to the relatively weak diffraction peaks of $AgIn_5S_8$ due to its poor crystal quality. The two reasons lead to cannot identify the $AgIn_5S_8$ phase in the composites through XRD technique. In the following, other characterization methods (DRS, SEM, TEM and

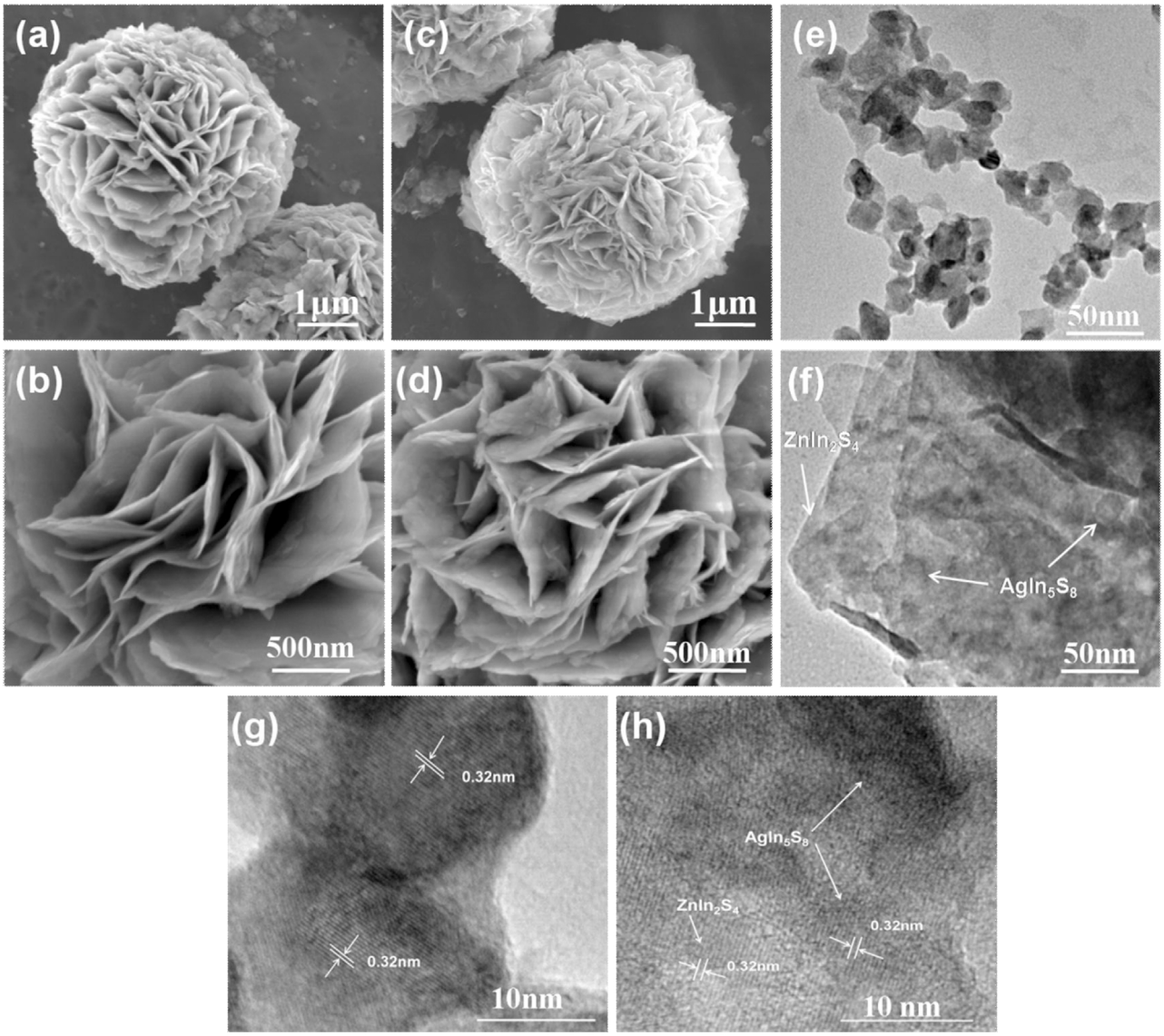

Fig. 3. SEM images of pure $ZnIn_2S_4$ (a and b) and 30%$AgIn_5S_8/ZnIn_2S_4$ composite (c and d). TEM images of $AgIn_5S_8$ (e) and 30%$AgIn_5S_8/ZnIn_2S_4$ composite (f). HRTEM images of $AgIn_5S_8$ (g) and 30%$AgIn_5S_8/ZnIn_2S_4$ composite (h).

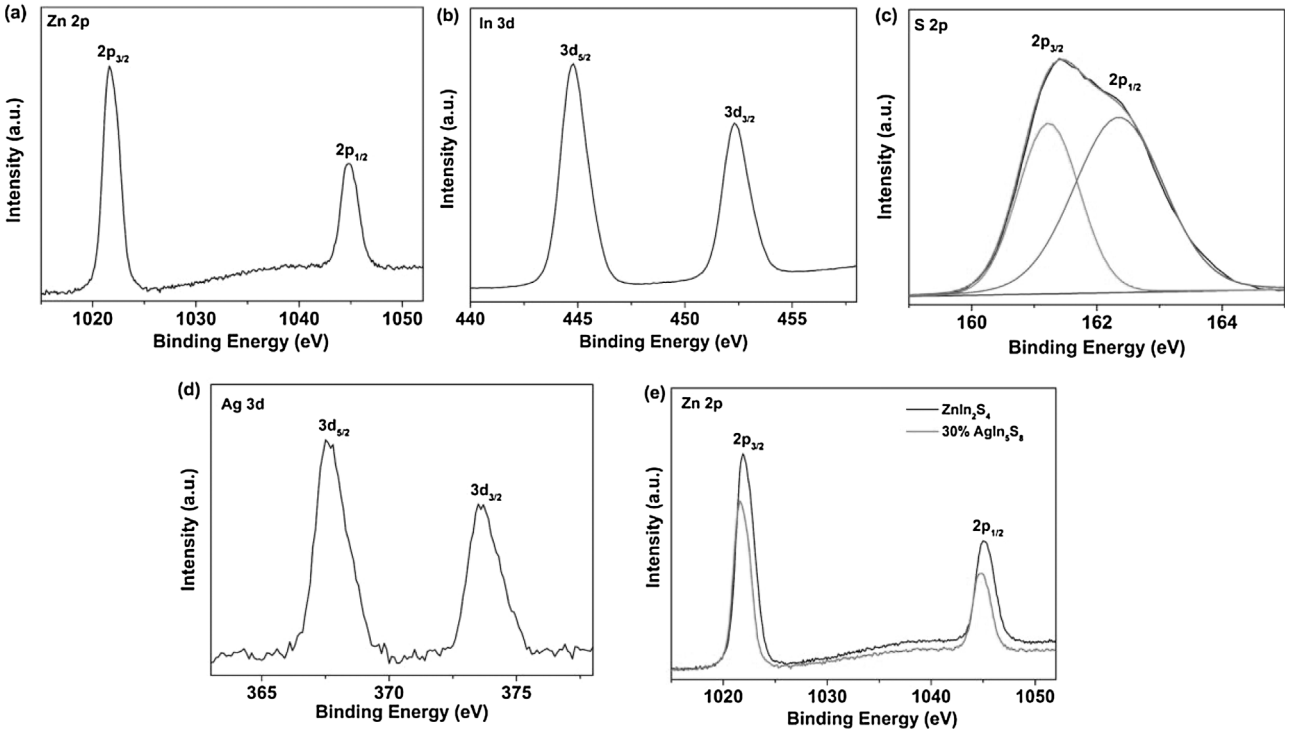

Fig. 4. XPS spectra of (a) Zn 2p, (b) In 3d, (c) S 2p and (d) Ag 3d for the 30%$AgIn_5S_8$/$ZnIn_2S_4$ composite sample. (e) XPS spectra of Zn 2p for the pure $ZnIn_2S_4$ and 30%$AgIn_5S_8$/$ZnIn_2S_4$ composite samples.

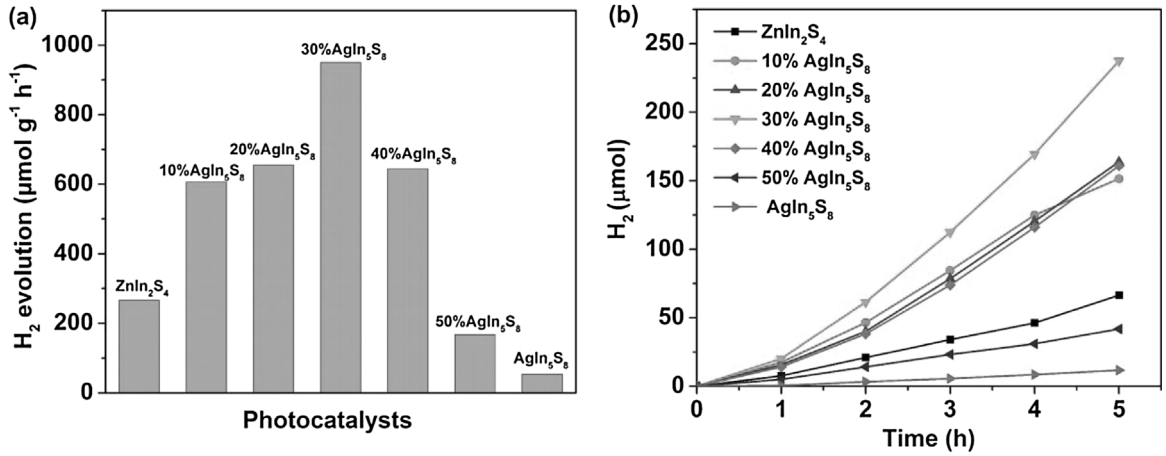

Fig. 5. (a) The H_2 evolution rates of pure $ZnIn_2S_4$, $AgIn_5S_8$ and $AgIn_5S_8$/$ZnIn_2S_4$ composites with different $AgIn_5S_8$ content under visible light irradiation (λ > 420). (b) Time courses of hydrogen evolution for pure $ZnIn_2S_4$, $AgIn_5S_8$ and $AgIn_5S_8$/$ZnIn_2S_4$ composites with different $AgIn_5S_8$ content under visible light irradiation (λ > 420).

XPS) were employed to detect $AgIn_5S_8$ in the composites.

The UV–vis diffuse reflectance spectra of pure $ZnIn_2S_4$, $AgIn_5S_8$ and $AgIn_5S_8$/$ZnIn_2S_4$ composites with different $AgIn_5S_8$ content are shown in Fig. 2. The absorption band edges of pure $ZnIn_2S_4$ is about 540 nm, corresponding to the band gap of 2.30 eV (see Fig. S1), which is in good agreement with the values reported previously [26,27]. For pure $AgIn_5S_8$, the absorption edge extends to about 750 nm and the estimated band gap is about 1.60 eV (see Fig. S1), which is close to the previous report [28]. The relatively small band gap of $AgIn_5S_8$ makes it can be used as a sensitizer to extend the visible-light response of $ZnIn_2S_4$. As it can be seen from Fig. 2, the absorption of the $AgIn_5S_8$/$ZnIn_2S_4$ composite in the visible-light region increases gradually with increasing the content of $AgIn_5S_8$. The enhanced visible-light absorption will be benefited to improve the photocatalytic H_2 evolution activity of $ZnIn_2S_4$.

The morphologies of $ZnIn_2S_4$ and 30%$AgIn_5S_8$/$ZnIn_2S_4$ composite were also characterized and the results are shown in Fig. 3. The pure $ZnIn_2S_4$ has a hierarchical microspheres structure with diameter range from about 3 μm to 7 μm (see Fig. 3(a) and Fig. S2). In Fig. 3(b), the hierarchical microsphere consists of ultrathin nanosheets with about 10–20 nm thickness. The ultrathin nanosheets surface is smooth. The unqiue 2D layer structure of $ZnIn_2S_4$ nanosheets can provide more contact areas when coupled with $AgIn_5S_8$ nanoparticles. After modified with $AgIn_5S_8$ nanoparticles, the hierarchical microsphere structure of $ZnIn_2S_4$ is not collapsed (see Fig. 3(c)). However, the ultrathin nanosheets surface becomes rough (see Fig. 3(d)). The result suggests that the $AgIn_5S_8$ nanoparticles are successfully anchored on the surface of $ZnIn_2S_4$ nanosheets. From Fig. 3(e), it can be seen that the $AgIn_5S_8$ nanoparticles sizes are about 10–25 nm. Some $AgIn_5S_8$ nanoparticles are agglomerated. In Fig. 3(f), the $AgIn_5S_8$ nanoparticles are uniformly dispersed on the surface of $ZnIn_2S_4$ nanosheets. In addition, an intimate contact between $AgIn_5S_8$ and $ZnIn_2S_4$ is formed, which will be in favour

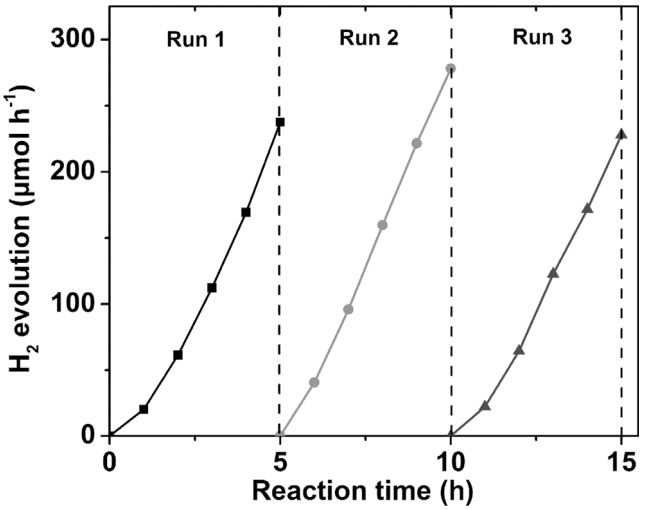

Fig. 6. Time course of H_2 evolution for the 30%$AgIn_5S_8$/$ZnIn_2S_4$ composite sample under visible light irradiation (λ > 420).

of the electrons transfering from $ZnIn_2S_4$ to $AgIn_5S_8$, and thus inhibiting the photogenerated the electron-hole pairs recombination in $ZnIn_2S_4$. The lattice fringes of ca. 0.32 nm in Fig. 3(g) is assigned to the (311) plane of $AgIn_5S_8$. In Fig. 3((h)), the lattice fringes of ca. 0.32 nm in the bright areas should come from the (102) plane of $ZnIn_2S_4$. While, in the dark areas, the lattice fringes of ca. 0.32 nm can be attributed to the (311) plane of $AgIn_5S_8$. Based on above DRS, SEM and TEM results analysis, it can be concluded that the $AgIn_5S_8$ /$ZnIn_2S_4$ 0D/2D heterojunction composite was obtained by a facile two-step hydrothermal process.

The surface element valence states of pure $ZnIn_2S_4$ and 30%$AgIn_5S_8$/$ZnIn_2S_4$ composite samples were measured and the results are shown in Fig. 4. In Fig. 4(a), the spectrum of Zn 2p presents two peaks with binding energies of 1021.6 eV and 1044.8 eV, which are assigned to the Zn^{2+} in $ZnIn_2S_4$ [29]. From Fig. 4(b), the binding energies of In $3d_{5/2}$ and In $3d_{3/2}$ locate at 444.8 eV and 452.3 eV, respectively, which are consistent with In^{3+} in $ZnIn_2S_4$ and/or $AgIn_5S_8$ [29,30]. The spectrum of S 2p shows two binding energy peaks at 161.2 eV and 162.2 eV in Fig. 4(c), which are in agreement with S^{2-} in $ZnIn_2S_4$ and/or $AgIn_5S_8$ [30,31]. In Fig. 4(d), the banding energies of Ag 3d are located at 367.5 eV and 573.7 eV, which can be ascribed to Ag^+ in the $AgIn_5S_8$ [32]. In addition, from Fig. 4(e), compared with pure $ZnIn_2S_4$, the peak of Zn 2p is shifted to the right for the 30%$AgIn_5S_8$/$ZnIn_2S_4$ composite sample. The peaks shift may be come from the strong electronic interaction and possible forming chemical bonding between $ZnIn_2S_4$ and $AgIn_5S_8$. Similar phenomenon was also observed for other heterojunctions in previous studies [33,34]. The real $AgIn_5S_8$ content in the 30%$AgIn_5S_8$/$ZnIn_2S_4$ sample was investigated by measuring Ag using the ICP-AES. The real weight ratio of $AgIn_5S_8$ to $ZnIn_2S_4$ is ca. 22.4% in the 30%$AgIn_5S_8$/$ZnIn_2S_4$ composite sample.

3.2. Photocatalytic H_2 evolution performance of photocatalysts

Fig. 5(a) shows the H_2 production rates of pure $ZnIn_2S_4$, $AgIn_5S_8$ and $AgIn_5S_8$/$ZnIn_2S_4$ composites with different $AgIn_5S_8$ content. Pure $ZnIn_2S_4$ exhibits a low hydrogen evolution rate of 265.9 μmol g^{-1} $(h)^{-}$

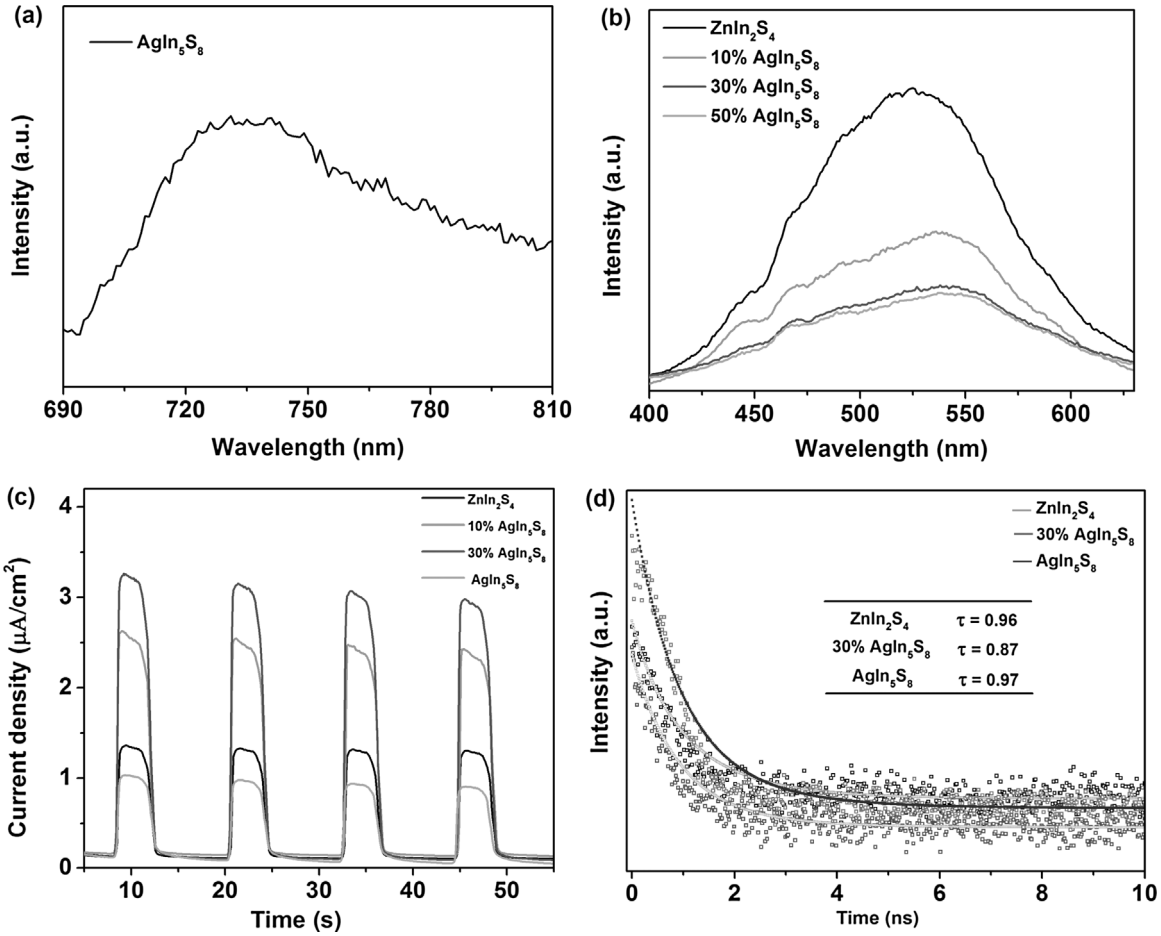

Fig. 7. (a) PL spectrum of $AgIn_5S_8$. (b) PL spectrum of pure $ZnIn_2S_4$ and $AgIn_5S_8$/$ZnIn_2S_4$ composites with different $AgIn_5S_8$ content. (c) Transient photocurrent responses of pure $ZnIn_2S_4$, $AgIn_5S_8$ and $AgIn_5S_8$/$ZnIn_2S_4$ composites with different $AgIn_5S_8$ content. (d) Time-resolved transient PL decay spectra of $ZnIn_2S_4$, 30%$AgIn_5S_8$/$ZnIn_2S_4$ and $AgIn_5S_8$ at room temperature.

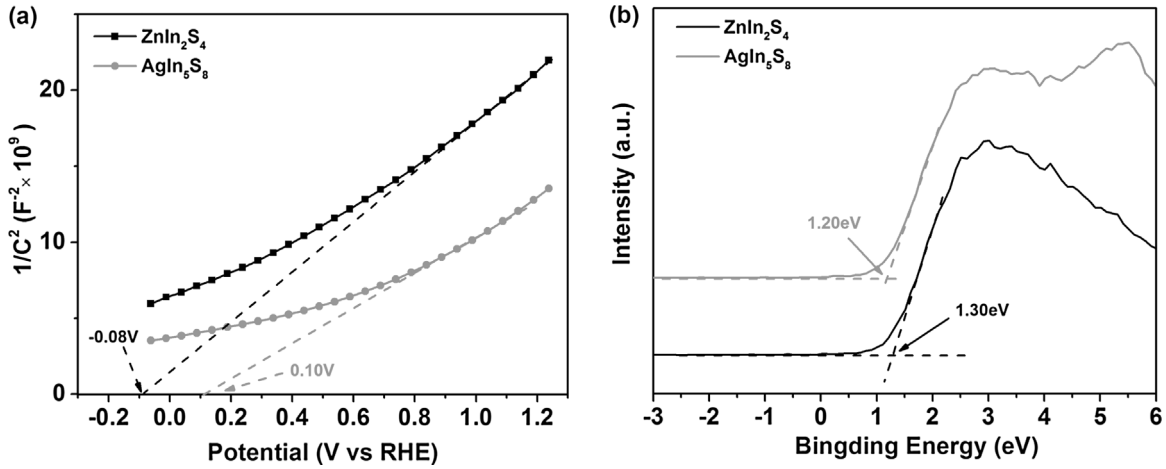

Fig. 8. (a) Mott-Schottky plots of $ZnIn_2S_4$ and $AgIn_5S_8$. (b) Valence-band XPS spectra of $ZnIn_2S_4$ and $AgIn_5S_8$.

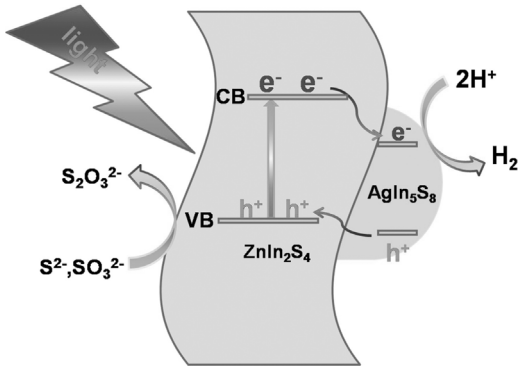

Fig. 9. Schematic illustration of hydrogen evolution process for the $AgIn_5S_8/ZnIn_2S_4$ composite under visible light irradiation.

$^{-1}$ due to the fast photoinduced electrons-holes pairs recombination and narrow visible light absorption. The pure $AgIn_5S_8$ also shows a low hydrogen production performance because of its poor crystallization quality and serious charge recombination. After coupled with the $AgIn_5S_8$ nanoparticles, a significant enhancement of H_2 production is achieved for the 10%$AgIn_5S_8/ZnIn_2S_4$ composite. The result suggests that the $AgIn_5S_8/ZnIn_2S_4$ 0D/2D heterojunction plays an important role for improving the photocatalytic performance. The charge recombination is efficiently inhibited through the 0D/2D heterojunction, which was confirmed by the following PL and photocurrent response results. For the $AgIn_5S_8/ZnIn_2S_4$ 0D/2D heterojunction, the relatively small sizes of $AgIn_5S_8$ nanoparticles provide abundant active sites for hydrogen evolution and shorten the charge-migration distance, while, the ultrathin $ZnIn_2S_4$ nanosheets provide large contact areas and prevent the $AgIn_5S_8$ nanoparticles agglomeration. When the content of $AgIn_5S_8$ increases to 30%, the highest H_2 evolution rate of 949.9 μmol g^{-1} $(h)^{-1}$ is obtained, which is about 3.6 and 17.6 times higher than pure $ZnIn_2S_4$ and $AgIn_5S_8$, respectively. If further increasing the content of $AgIn_5S_8$, the H_2 production performance decreases. This phenomenon can be ascribed the fact that $AgIn_5S_8$ nanoparticles are easily aggregated under high content and pure $AgIn_5S_8$ nanoparticles show low H_2 evolution activity. The time courses of hydrogen evolution for pure $ZnIn_2S_4$, $AgIn_5S_8$ and $AgIn_5S_8/ZnIn_2S_4$ composites with different $AgIn_5S_8$ content are shown in Fig. 5(b). The amount of H_2 evolution with reaction time exhibits a nearly linear trend for the different samples. The stability of H_2 evolution for the composite photocatalyst is also important for practical application. The time course of H_2 evolution for the 30%$AgIn_5S_8/ZnIn_2S_4$ composite sample was evaluated and the results are shown in Fig. 6. After the second-cycle test finished, the amount of evolution H_2 is slight higher than the first-cycle test, which possibly come from some Pt cocatalyst further depositing the surface of composite under irradiation. Compared with the first-cycle test, no obvious decrease of the H_2 evolution is observed after 15 (h) reaction, which indicates that the composite is relatively stable during the solar hydrogen evolution reaction. The methanol was also chose as sacrificial agent to evaluate the H_2 evolution performance of 30%$AgIn_5S_8/ZnIn_2S_4$ composite sample and the results are shown in Fig. S3. A very low H_2 evolution rate of 12.69 μmol g^{-1} $(h)^{-1}$ is obtained. In addition, the H_2 evolution rate decreases about 34% after 15 (h) reaction. This results suggest that methanol is not an ideal sacrificial agent for the $AgIn_5S_8/ZnIn_2S_4$ composite due to its low oxidation potential [35].

3.3. Mechanism for enhanced photocatalytic performance of $AgIn_5S_8/ZnIn_2S_4$ 0D/2D heterojunction composite

Besides enhanced visible-light absorption (see Fig. 2), the improved charge separation is another probable reason for the enhanced H_2 production performance. PL characterization is usually used to evaluate the charge separation efficiency [36,37]. Therefore, the PL spectra of pure $ZnIn_2S_4$, $AgIn_5S_8$ and $AgIn_5S_8/ZnIn_2S_4$ composites with different $AgIn_5S_8$ content were measured and the results are shown in Fig. 7(a) and Fig. 7(b). The emission peak for the band gap transition of $AgIn_5S_8$ nanoparticles locates at about 734 nm [28]. In Fig. 7(b), all samples show a strong emission peak the about 525 nm, which can be assigned to the band gap transition of $ZnIn_2S_4$ [38]. Pure $ZnIn_2S_4$ shows the strongest PL spectra intensity, which indicates the fastest charge recombination. Remarkably, the PL intensity of $ZnIn_2S_4$ significantly decreases with increasing the content of $AgIn_5S_8$. The result suggests that the charge recombination in $ZnIn_2S_4$ is efficiently suppressed when integrated with the $AgIn_5S_8$ nanoparticles. In order to further confirm the charge transfer process, the photocurrent responses of pure $ZnIn_2S_4$, $AgIn_5S_8$ and $AgIn_5S_8/ZnIn_2S_4$ composites with different $AgIn_5S_8$ content were recorded and the results are indicated in Fig. 7(c). The schematic diagram of a photoelectrochemical cell for the $AgIn_5S_8/ZnIn_2S_4$ photoelectrode is plotted in Fig. S4. Pure $ZnIn_2S_4$ and $AgIn_5S_8$ show low photocurrent. After designing the 0D/2D heterojunction, the 10% $AgIn_5S_8/ZnIn_2S_4$ composite sample shows an obvious enhanced photocurrent. The 30% $AgIn_5S_8/ZnIn_2S_4$ composite exhibits the highest photocurrent, which is in good agreement with the H_2 evolution activity (see Fig. 5(a)). The result indicates that the 0D/2D heterojunction improves the charge transfer for $ZnIn_2S_4$. The time-resolved transient PL decay spectra of $ZnIn_2S_4$, 30%$AgIn_5S_8/ZnIn_2S_4$ and $AgIn_5S_8$ are shown in Fig. 7(d). The average lifetimes of photogenerated charges were determined to be 0.96, 0.87 and 0.97 ns for $ZnIn_2S_4$, 30%$AgIn_5S_8/ZnIn_2S_4$ and $AgIn_5S_8$, respectively (see Table S1). The 30%$AgIn_5S_8/ZnIn_2S_4$ sample has the shortest average lifetime of charges, indicating

efficient charge separation [39,40]. According to above discussion, it is obvious that the improved charge separation efficiency and enhanced visible-light absorption can be attributed to the improved H_2 evolution performance of $AgIn_5S_8/ZnIn_2S_4$ composite.

The precise conduction and valence band positions of the $ZnIn_2S_4$ nanosheet and $AgIn_5S_8$ nanoparticle were determined by Mott-Schottky and valence-band XPS spectra (see Fig. 8). $ZnIn_2S_4$ and $AgIn_5S_8$ are both show an n-type semiconductor character. The flat band positions of $ZnIn_2S_4$ and $AgIn_5S_8$ are about -0.08 V and 0.10 V vs RHE, respectively. The valence band maximum positions of $ZnIn_2S_4$ and $AgIn_5S_8$ are 1.20, and 1.30 V, respectively. The band gaps of $ZnIn_2S_4$ and $AgIn_5S_8$ are calculated to be about 2.30 eV and 1.60 eV according to the UV–vis DRS spectra, respectively (see Fig. S1). Based on these results, the conduction band (CB) and valence band (VB) of $ZnIn_2S_4$ are -1.08 V and 1.22 V vs RHE, respectively, and the CB and VB of $AgIn_5S_8$ locate at about -0.30 V and 1.30 V, respectively, which are similar to previous reported [12,41]. Therefore, the $AgIn_5S_8/ZnIn_2S_4$ composite forms a type-II heterojunction, which will be benefited to enhance the photogenerated charges separation efficiency. In order to understand the hydrogen evolution process for the $AgIn_5S_8/ZnIn_2S_4$ composite under visible light irradiation, a schematic illustration was drawn in Fig. 9. Under visible light irradiation, the photoexcited electrons in $ZnIn_2S_4$ nanosheets would transfer to the CB of $AgIn_5S_8$ nanoparticles and then are injected into Pt cocatalyst to reduce protons into H_2. Meanwhile, the holes in $AgIn_5S_8$ nanoparticles will migrate to $ZnIn_2S_4$ nanosheets, which can be efficiently quenched by the sacrificial reagent.

4. Conclusions

In summary, the $AgIn_5S_8/ZnIn_2S_4$ 0D/2D heterojunction composites were prepared via a facile two-step hydrothermal process. The highest H_2 production rate of 949.9 μmol g^{-1} h^{-1} was obtained over the 30%$AgIn_5S_8/ZnIn_2S_4$ composite sample, which is about 3.6 and 17.6 times higher than pure $ZnIn_2S_4$ and $AgIn_5S_8$, respectively. The 0D/2D heterojunction composite exhibited excellent photocatalytic H_2 production performance due to its improved charge separation, as well as the enhanced visible-light absorption. This study indicates that constructing a 0D/2D heterojunction is a promising way to improve the photocatalytic H_2 evolution performance of photocatalysts.

Acknowledgments

The authors gratefully acknowledge the support of the National Natural Science Foundation of China (51702087, 21673066 and 21703054), Program for Science & Technology Innovation Talents (15HASTIT043) and Innovative Research Team (16IRTSTHN015) from the University of Henan Province.

Appendix A. Supplementary data

Supplementary material related to this article can be found, in the online version, at doi:https://doi.org/10.1016/j.apcatb.2018.01.068.

References

[1] M. Grätzel, Nature 414 (2001) 338–344.
[2] A. Kudo, Y. Miseki, Chem. Soc. Rev. 38 (2009) 253–278.
[3] H. Tong, S. Ouyang, Y. Bi, N. Umezawa, M. Oshikiri, J. Ye, Adv. Mater. 24 (2012) 229–251.
[4] A. Fujishima, K. Honda, Nature 238 (1972) 37–38.
[5] Z. Zou, J. Ye, K. Sayama, H. Arakawa, Nature 414 (2001) 625–627.
[6] Q. Wang, T. Hisatomi, Q. Jia, H. Tokudome, M. Zhong, C. Wang, Z. Pan, T. Takata, M. Nakabayashi, N. Shibata, Y. Li, I.D. Sharp, A. Kudo, T. Yamada, K. Domen, Nat. Mater. 15 (2016) 611–615.
[7] Z. Lei, W. You, M. Liu, G. Zhou, T. Takat, M. Hara, K. Domen, C. Li, Chem. Commun. (2003) 2142–2143.
[8] J. Wang, Y. Chen, W. Zhou, G. Tian, Y. Xiao, H. Fu, H. Fu, J. Mater. Chem. A 5 (2017) 8451–8460.
[9] L. Shang, C. Zhou, T. Bian, H. Yu, L. Wu, C. Tung, T. Zhang, J. Mater. Chem. A 1 (2013) 4552–4558.
[10] Z. Wu, C. Gong, J. Yu, L. Sun, W. Xiao, C. Lin, J. Mater. Chem. A 5 (2017) 1292–1299.
[11] J. Hou, C. Yang, H. Cheng, Z. Wang, S. Jiao, H. Zhu, Phys. Chem. Chem. Phys. 15 (2013) 15660–15668.
[12] Z. Zhang, K. Liu, Z. Feng, Y. Bao, B. Dong, Sci. Rep. 6 (2016) 19221.
[13] A. Boulesbaa, K. Wang, M. Mahjouri-Samani, M. Tian, A.A. Puretzky, I. Ivanov, C.M. Rouleau, K. Xiao, B.G. Sumpter, D.B. Geohegan, J. Am. Chem. Soc. 138 (2016) 14713–14719.
[14] M. Ye, Z. Zhao, Z. Hu, L. Liu, H. Ji, Z. Shen, T. Ma, Angew. Chem. Int. Ed. 56 (2017) 1–6.
[15] D. Chen, J. Ye, J. Phys. Chem. Solids 68 (2007) 2317–2320.
[16] K. Li, B. Chai, T. Peng, J. Mao, L. Zan, ACS Catal. 3 (2013) 170–177.
[17] X. Liu, H. Chen, R. Wang, Y. Shang, Q. Zhang, W. Li, G. Zhang, J. Su, C.T. Dinh, F. de Arquer, J. Li, J. Jiang, Q. Mi, R. Si, X. Li, Y. Sun, Y. Long, H. Tian, E.H. Sargent, Z. Ning, Adv. Mater. 29 (2017) 1605646.
[18] Y. Jin, D. Jiang, D. Li, M. Chen, Catal. Sci. Technol. 7 (2017) 2308–2317.
[19] J. Ran, X. Wang, B. Zhu, S. Qiao, Chem. Commun. 53 (2017) 9882–9885.
[20] L. Yao, D. Wei, Y. Ni, D. Yan, C. Hu, Nano Energy 26 (2016) 248–256.
[21] Q. Li, C. Cui, H. Meng, J. Yu, Chem. Asian J. 9 (2014) 1766–1770.
[22] G. Gong, Y. Liu, B. Mao, L. Tan, Y. Yang, W. Shi, Appl. Catal. B: Environ. 216 (2017) 11–19.
[23] B. Chai, T. Peng, P. Zeng, X. Zhang, X. Liu, J. Phys. Chem. C 115 (2011) 6149–6155.
[24] Y. Chen, S. Hu, W. Liu, X. Chen, L. Wu, X. Wang, P. Liu, Z. Li, Dalton Trans. 40 (2011) 2607–2613.
[25] K. Li, J. Xu, X. Zhang, T. Peng, X. Li, Int. J. Hydrogen Energy 38 (2013) 15965–15975.
[26] J. Chen, F. Xin, X. Yin, T. Xiang, Y. Wang, RSC Adv. 5 (2015) 3833–3839.
[27] L. Zhang, W. Zhang, H. Tao, G. Wang, J. Ma, Q. Wang, M. Tan, S. Xu, CrystEngComm 19 (2017) 3619–3625.
[28] S. Song, Z. Liang, W. Fu, T. Peng, ACS Appl. Mater. Interfaces 9 (2017) 17013–17023.
[29] J. Hou, C. Yang, H. Cheng, Z. Wang, S. Jiao, H. Zhu, Phys. Chem. Chem. Phys. 15 (2013) 15660–15668.
[30] J. Song, T. Jiang, G. Ji, W. Zhang, X. Cheng, W. Weng, L. Zhu, X. Xu, RSC Adv. 5 (2015) 95943–95952.
[31] L. Ye, J. Fu, Z. Xu, R. Yuan, Z. Li, ACS Appl. Mater. Interfaces 6 (2014) 3483–3490.
[32] W. Zhang, D. Li, M. Sun, Y. Shao, Z. Chen, G. Xiao, X. Fu, J. Solid State Chem. 183 (2010) 2466–2474.
[33] F. Zhang, X. Li, Q. Zhao, Aicheng Chen, J. Phys. Chem. C 120 (2016) 19113–19123.
[34] D. Ma, J. Shi, Y. Zou, Z. Fan, X. Ji, C. Niu, ACS Appl. Mater. Interfaces 9 (2017) 25377–25386.
[35] M.J. Berr, P. Wagner, S. Fischbach, A. Vaneski, J. Schneider, A.S. Susha, A.L. Rogach, F. Jäckel, J. Feldmann, Appl. Phys. Lett. 100 (2012) 223903.
[36] Z. Guan, P. Wang, Q. Li, Y. Li, X. Fu, J. Yang, Chem. Eng. J. 327 (2017) 397–405.
[37] Y. Yuan, D. Chen, J. Zhong, L. Yang, J. Wang, M. Liu, W. Tu, Z. Yu, Z. Zou, J. Mater. Chem. A 5 (2017) 15771–15779.
[38] Y. Yuan, J. Tu, Z. Ye, D. Chen, B. Hu, Y. Huang, T. Chen, D. Cao, Z. Yu, Z. Zou, Appl. Catal. B: Environ. 188 (2016) 13–22.
[39] D. Zhao, J. Chen, C. Dong, W. Zhou, Y. Huang, S.S. Mao, L. Guo, S. Shen, J. Catal. 352 (2017) 491–497.
[40] Y. Chen, Y. Pu, Y. Hsu, J. Phys. Chem. C 116 (2012) 2967–2975.
[41] K. Cheng, S. Wang, Mater. Chem. Phys. 115 (2009) 14–20.